IEEE Access
Multidisciplinary | Rapid Review | Open Access Journal

Received 13 May 2024, accepted 26 May 2024, date of publication 6 June 2024, date of current version 25 June 2024.

Digital Object Identifier 10.1109/ACCESS.2024.3410698

RESEARCH ARTICLE

A Novel Dual-Channel SPR-Based PCF Biosensor for Simultaneous Tuberculosis and Urinary Tract Infection Diagnosis Toward SDG3

J. DIVYA[1], S. SELVENDRAN[1,2], SRIKANTH ITAPU[3], AND VAMSI BORRA[4], (Senior Member, IEEE)

[1]School of Electronics Engineering (SENSE), Vellore Institute of Technology, Chennai 600127, India
[2]Centre for Healthcare Advancement, Innovation and Research (CHAIR), Vellore Institute of Technology, Chennai 600127, India
[3]Department of ECE, Alliance College of Engineering and Design, Alliance University, Bengaluru, Karnataka 562106, India
[4]Electrical and Computer Engineering Program, Youngstown State University, Youngstown, OH 44555, USA

Corresponding author: S. Selvendran (selvendran.s@vit.ac.in)

ABSTRACT Sustainable development goal (SDG) 3.3 targets the eradication of epidemics such as AIDS, Tuberculosis (TB), hepatitis, and other communicable diseases. Effective early disease detection methods are essential for reaching this objective. Surface plasmon resonance (SPR) influenced biosensors are now widely recognized as an effective method for detecting biomolecular interactions in real time, without the need for labeling. This study proposes a dual-channel photonic crystal fiber (PCF)-based SPR sensor for simultaneous detection of two different analytes. The sensor features channels Ch1 and Ch2, each with unique resonance peaks at different wavelengths corresponding to the refractive index (RI) of the sensing samples. The sensor's structure is optimized using Finite Element Method (FEM), ensuring high sensitivity and a rapid response within the RI range of bio-analytes. RI data sourced from infectious diseases like Tuberculosis (TB) and Urinary Tract Infection (UTI) are utilized. Initially, Ch1 focuses on TB detection, and Ch2 on UTI detection, achieving optimal wavelength sensitivity of 10,000 nm/RIU and 8235.29 nm/RIU for Ch1 and Ch2, respectively. Notably, both channels excel at distinguishing samples of the same disease. When detecting TB, these channels exhibit distinct resonance wavelengths for heavily and mildly infected blood samples, demonstrating remarkable sensitivity of 32,000 nm/RIU. Similarly, for UTI detection, the biosensor achieves a sensitivity of 73,170 nm/RIU when distinguishing between gram-positive and gram-negative bacteria. The sensor's performance is evaluated based on sensing resolution, sensitivity, and figure of merit values, demonstrating its potential for accurate and early diagnosis of TB and UTIs.

INDEX TERMS Photonic crystal fiber, surface plasmon resonance, biosensor, gold, silver, graphene, titanium dioxide, tuberculosis, urinary tract infections, sustainable development goal.

I. INTRODUCTION

TB is a highly contagious disease caused by Mycobacterium tuberculosis bacteria, primarily affecting the lungs but can also other parts of the body. It spreads through the air when infected individuals cough, sneeze, or talk. TB is a major global health concern, ranking thirteenth among infectious diseases in mortality [1]. As per the World Health Organization (WHO) report of 2021, there were 10.6 million new TB cases and 1.6 million deaths globally. Developing countries, particularly in South East Asia, contribute to almost 46% of the worldwide TB cases. In 2021, India alone reported 2.14 million cases, which is 18% higher than the previous year [2], [3], [4]. In response to these alarming statistics, the WHO initiated the End Tuberculosis strategy in 2015, aiming to substantially reduce new TB cases by 2025 and eliminate the global TB epidemic by 2035 [5]. This aligns with SDG 3.3, targeting the end of epidemics, including TB. Traditional TB detection methods like chest radiology, swab culturing, and bacterioscopy are often imprecise or time-consuming, demanding skilled personnel and advanced lab facilities. This poses challenges, particularly for developing nations. Recent advancements, like GeneXpert PCR, ELISA, and Radiometric tests targeting TB DNA [6],

The associate editor coordinating the review of this manuscript and approving it for publication was San-Liang Lee.

[7], offer promise. However, these methods still require sample preparation time and access to advanced laboratory facilities.

UTIs are significant bacterial infections affecting the kidneys, bladder, urethra, and ureters [8]. They can be caused by both gram-positive and gram-negative microorganisms, with Escherichia coli (E. coli) being the most common gram-negative bacterium, typically found in the gastrointestinal tract. Other bacteria contributing to UTIs include Enterococcus faecalis (E.faecalis), Pseudomonas aeruginosa, Klebsiella pneumoniae, and Staphylococcus saprophyticus [9], [10]. Globally, approximately 150 million people are affected by UTIs each year, with women being more susceptible than men [10], [11]. UTI is frequently encountered during pregnancy, due to the anatomical and physiological variations that take place in the genitourinary tract [12]. According to studies conducted in India, approximately 3% to 24% of pregnant women are affected by the UTI [13]. The high prevalence of UTIs during pregnancy can lead to various complications, including hypertensive disorders, premature birth, anemia, chronic kidney failure, and low birth weight infants [14]. The timely identification and treatment of UTIs are crucial in minimizing maternal morbidity and the risk of recurrence, while also decreasing the chances of premature birth and fetal mortality in the baby [15].

Traditionally, UTI diagnosis relied on conventional techniques like urine microscopy, culturing, and Isothermal microcalorimetry [16]. In clinical trials, urine culturing is a cost-effective method, it is labor-intensive, time-consuming, and requires specific growth media [17]. To overcome these challenges, rapid detection methods such as ELISA [18], and PCR [19] are used. Despite reducing analysis time, these techniques still demand skilled pathologists and expensive equipment for pathogen extraction and examination. Consequently, there's a growing demand for reliable, simple, rapid, cost-effective, and highly sensitive diagnostic tools for both TB and UTI, leading to the development of biosensors [20].

SPR-based sensors offer advantages over conventional sensors for detecting biological interactions. SPR is a quantum optical process enabling direct and sensitive detection of biomolecular interactions without fluorescent labels [21]. In an SPR-based sensor, a thin metal film serves a dual role—hosting biomolecular probes on one side and interacting with infrared light on the other, creating a minimum reflected light intensity at a specific angle. Target molecules interacting with the probes induce changes in optical properties, altering the angle. A linear ray detector translates the reflected light profile into an electrical signal, revealing biochemical interactions in samples as small as a few nanograms [22]. SPR finds diverse applications, encompassing the assay of antibodies, antigens, bacteria, viruses, DNA, RNA, hemoglobin, hormones, and proteins, with potential future applications [23], [24], [25], [26]. This label-free detection method offers high specificity and sensitivity, and enables real-time monitoring of biomolecular interactions. In addition, SPR sensors provide numerous advantages, including exceptional accuracy, rapid analysis times, and low detection limits, rendering them highly valuable for a wide range of applications [27], including biosensing [28], chemical sensing [29], and environmental monitoring [30]. However, SPR based sensors have a several advantages, it cannot be used in remote sensing applications because of its bulky size, and the cost of this sensor is also high [31].

Optical fiber-based SPR sensors have been developed as a solution to the issue, and they are suitable for remote sensing applications due to their small size, flexibility, and high precision [32]. In 2022, Chiavaioli et al. introduced a novel sensor design utilizing a D-shaped optical fiber for the detection of Alzheimer's disease (AD) biomarkers. Tin dioxide (SnO_{2-x}) was coated onto a cleaved region of the D-shaped fiber, generating a leaky mode resonance (LMR). This proposed sensor demonstrated an average RI sensitivity ranging from 4 to 8 μm^1 RIU, superior that of conventional optical fiber-based sensors [33]. In that year, Zhu et al. proposed a plasmonic fiber sensor designed to detect tumor cells (TC) in blood samples. This sensor incorporated two types of fibers: a multi-mode fiber (MMF) for light transmission and a single-mode fiber (SMF) coated with gold for TC sensing. Gold coating at the fiber's end triggered a SPR effect to facilitate light transmission. The proposed fiber probe sensor achieved a sensitivity of 1933.4 nm/RIU across a RI range of 1.33-1.37 [34]. However, metallization of the fiber structure can lead to a degradation of its structural integrity as it is done on the cladding portion, and thus the fiber needs to be polished up to the core portion, and this makes the fabrication process more complex. To address this problem, PCF-based SPR sensors have been developed, which involve coating or filling the specific air holes with metals [35]. Unlike conventional fibers, PCF have a unique optical property, such as high birefringence, low transmission loss, strong non-linearity, endless single mode, and the ability to control light propagation [36], so this makes PCF based SPR sensors are the power tool for detecting minute changes of the biochemical molecules (analyte).

A PCF-based SPR sensor's functionality depends on the interaction of the core mode and plasmon mode, which happens when light of a certain wavelength interacts with a metal surface [37]. Through this interaction, the core mode creates a leaky mode that allows energy to be transferred from the core mode to the plasmon mode. The resonance wavelength is the wavelength at which this transfer happens, and it establishes a phase-matching condition [38]. The resonant wavelength of the sensor shifts due to the changes in the RI of the analyte near the metal surface, which results in improved accuracy and sensitivity of the sensor. Rahaman et al., created an SPR sensor by incorporating a PCF to measure glucose levels in urine samples. In order to create the SPR phenomena, the fiber's cladding area was covered with a thin coating of gold (Au), and the sensor was immersed in the sample for analysis. The maximum sensitivity achieved by the sensor was 152 RIU^{-1} for amplitude and 2500 nm/RIU for wave-

length [39]. In order to detect RI across a broad range, Deepak Kumar et al. provided a PCF-based SPR sensor. Silver was used as the plasmonic material and the greatest amplitude sensitivity of 1932.09 RIU-1 within the RI range of 1.25 to 1.30 [40].

The use of single analyte detection method is prevalent in PCF-based SPR sensors, but they have certain drawbacks such as low selectivity, longer detection time, and the inability to distinguish between multiple analytes at the same time. To address these issues, multi-channel PCF-based plasmonic sensors have been created, which can detect multiple analytes simultaneously and in parallel [41]. Utilizing multi-channel sensors enables the detection of multiple analytes concurrently, enhancing sensor efficiency. Moreover, these sensors mitigate potential detection errors related to varying detection times [42]. A multi-channel SPR sensor with two channels, Ch1 and Ch2, was presented by Yasli et al. in 2020. The sensor exhibited an optimal wavelength sensitivity of 2500 nm/RIU for Ch1 and 3083 nm/RIU for Ch2. The sensor's channels were covered with a plasmonic coating consisting of Au and silver (Ag), with graphene added on top of the silver layer to enhance sensitivity and prevent oxidation [41]. In order to increase sensitivity and selectivity, Mustafizur Rahman et al. proposed a multi-channel SPR sensor in 2021 that included three channels, each of which was coated with a different material: Au, Au with Tantalum Pentoxide (Ta_2O_5), and Au with Titanium dioxide (TiO_2). The sensor demonstrated greatest wavelength sensitivities of 38100 and 21600 nm/RIU for Ch1 and Ch2, respectively. For Ch3, the sensor achieved a maximal sensitivity of 45800 nm/RIU [43].

Previous studies have highlighted the unique features of multi-channel SPR sensors, showcasing their potential for diverse sensing applications. Building upon this research, this work presents a dual-channel PCF-based SPR sensor with high sensitivity. This sensor specifically targets the detection of bacteria responsible for both TB and UTIs. The sensor features a simple design comprising two sensing channels located within the cladding region. Each sensing channel's inner surface is coated with gold and graphene for Ch1 and silver and Titanium dioxide (TiO_2) for Ch2. These coatings serve to induce the plasmonic effect and enhance sensing performance. When the analyte, i.e., the bacteria of interest, is introduced into the sensing channels, it alters the effective RI of the sensor structure. This leads to a shift in the resonance wavelength, which can be detected and analyzed. The proposed sensor demonstrates the capability to detect both TB and UTI bacteria simultaneously. Numerical investigations are carried out using the FEM to analyze the performance of proposed sensor. Through the optimization of structural parameters, the sensor achieves impressive performance metrics, possessing a maximum wavelength sensitivity of 32,000 nm/RIU for TB detection and 73,170 nm/RIU for UTI detection. With its enhanced sensing capabilities, the proposed dual-channel PCF-based SPR biosensor holds significant promise for the early diagnosis of TB and UTIs. In addition, Section II outlines the fundamental theories and the design of the proposed sensor, while Section III explores various structural parameter optimizations and their corresponding results. Lastly, Section IV draws conclusions from the outcomes and findings of the proposed.

II. PROPOSED SENSOR GEOMETRY AND NUMERICAL INVESTIGATION

Fig. 1(a) depicted the graphical representation of the proposed dual-channel PCF based SPR sensor. The structure is composed of five sections: the innermost layer comprises the core, followed by the cladding region, the plasmonic layer, the sensing channels, and the outermost section, which is a perfectly matched layer (PML) specifically designed to absorb reflected light and minimize scattering losses. In this structure, a circularly arranged hexagonal lattice of air holes is positioned on a silica substrate. Four different sizes of air holes, with diameters d1 = 1.4μm, d2 = 1μm, d3 = 0.8μm, and d4 = 0.5μm, are intentionally used. The purpose of this deliberate arrangement is to enable a controlled leakage of light towards the plasmon layer, thereby enhancing the coupling efficiency. To induce the SPR effect, Ch1 utilizes a 0.04 μm thick layer of gold (t_{Au}), while Ch2 uses a silver layer (t_{Ag}). The performance of the sensor is enhanced by applying a 0.01 μm thickness graphene coating ($t_{graphene}$) and TiO_2(t_{TiO2}) coating on gold and silver layers respectively. This configuration achieves a dual purpose of improving the sensor's performance while also preventing oxidation of the metals. The sensor has two sensing channels with a thickness ($t_{sensingchannels}$) of 1.5 μm each. The upper channel is designated as Ch1 and the lower one as Ch2. The inner walls of Ch1 are coated with gold and graphene layers, while the inner walls of Ch2 are coated with silver and TiO_2 layers. The gap between two channels ($d_{channelgap}$) is fixed as 1 μm. The application of scattering boundary conditions, along with a 1 μm thick PML in the outer region, effectively reduces energy reflection. The sensor is designed with a total diameter of 16 μm, resulting in a compact design that facilitates efficient usage and integration.

The proposed dual-channel PCF based SPR sensor could be fabricated using stack and draw method [44], [45]. Electroless plating techniques enable the deposition of plasmon layers on the inner wall of the fiber [46], offering a valuable method for depositing metal to concealed areas within complex structures. Other plasmonic metals such as graphene and TiO_2 can also be coated through high-pressure chemical vapor deposition [47], yielding a uniform thin nanolayer, or through electron beam evaporation, which is a type of physical vapor deposition. Electron beam evaporation ensures high purity and precision in metal deposition by utilizing an electromagnetic field. Moreover, the electron beam evaporator allows for precise control over the thickness of the metal film [48]. Finally, an infiltration method can be utilized to inject the analyte into the sensing channels [49]. Numerical analysis is conducted using the FEM method, employing a

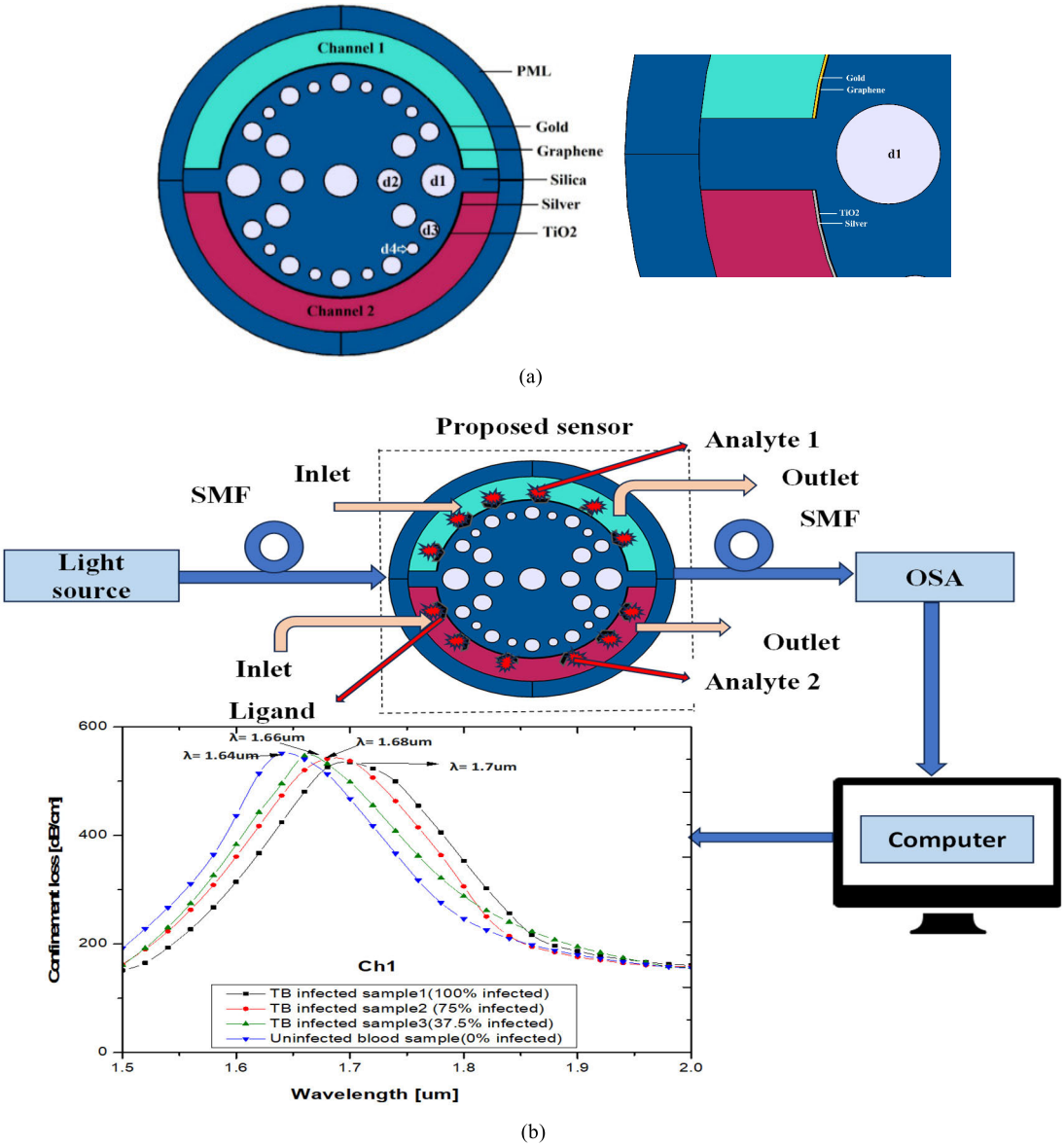

(a)

(b)

FIGURE 1. (a) Schematic representation of the proposed dual-channel PCF based SPR sensor; (b) The proposed sensor setup under experimental conditions.

physics-controlled mesh model to finely mesh the sensor's structure. The mesh consists of elements with a maximum size of 0.569 μm and a minimum size of 0.0012 μm. The maximum element growth rate is set to 1.2, and the curvature factor is 0.25.

Fig. 1(b) depicts the setup of the proposed dual channel D-shaped sensor used in the experiment. The coupling efficiency is enhanced by introducing a light source with a wide spectrum into the sensor through a single mode fiber (SMF). The light is incident in the proposed sensor at the air-core interface and guided within the core (core1 and core2) through the principle of modified total internal reflection (MTIR). SPR occurs at the interface between a metal surface and a medium containing an analyte. When a specific molecule is detected, the metal surface undergoes a RI modification, causing an alteration in the effective RI of the sensor structure and resulting in a wavelength shift. In this method, SPR sensors exhibit a reflectance dip due to energy transfer from core to the plasmon surface, displaying sensitivity to changes in the surrounding dielectric medium. These changes can be detected by connecting an optical spectrum analyzer (OSA) to a computer. Analyzing the data received from the computer allows the determination of the RI of the unknown analyte. Reproducibility in a PCF sensor refers to its ability to consistently generate reliable results when detecting the same analyte under comparable experimental conditions. The proposed sensor demonstrates good reproducibility, facilitated by the inclusion of both inlet and outlet pathways within the channel, making the process of filling and emptying the channel more efficient. This design enables versatile reuse in a variety of analyses involving analytes with diverse refractive indexes.

A. BASIC THEORY

The Sellmeier equation is used to determine the RI of silica, which is used as the core material in the proposed sensor [50].

$$n(\lambda)^2 = 1 + \frac{A_1\lambda^2}{\lambda^2 - \lambda_1^2} + \frac{A_2\lambda^2}{\lambda^2 - \lambda_2^2} + \frac{A_3\lambda^2}{\lambda^2 - \lambda_3^2}$$

where, A1 = 0.696 1663, A2 = 0.407 9426, A3 = 0.897 479, λ1 = 0.068 404, λ2 = 0.116 2414, λ3 = 9.896 161 are the Sellmeier constants and λ is the operating wavelength in μm.

Gold and silver are chosen as the plasmonic material due to its excellent optical characteristics, stability, and biocompatibility. The Drude model is often used to estimate the dispersion behavior of gold at various wavelengths. Mathematically, it can be represented as follows [50] and [51],

$$\varepsilon_{Au} = 1 - \frac{\omega_p^2}{w^2 + i\omega\Gamma p}$$

where ω- operating frequency, plasma frequency $\omega_P = 9.06eV$ and damping rate $\Gamma_P = 0.07eV$.

$$\varepsilon_{Ag} = 1 - \frac{\lambda^2\lambda_C}{\lambda_p^2(\lambda_c + i\lambda)}$$

where, collision wavelength λc = 17.614 μm, Plasma wavelength λp = 0.14541 μm, and λ being the free space wavelength in μm.

Graphene and TiO_2 are utilized as an adhesive layer to establish a connection between the plasmonic metal and the fiber surface. This adhesive layer enhances the coupling efficiency between the fundamental mode and plasmon modes, while also providing protection against oxidation of the plasmonic metals. The following equations are employed to determine the RI of graphene [52] and TiO_2 [38],

$$n_{graphene} = \frac{3 + iC_1\lambda}{3}$$

$$n^2(TiO_2) = 5.913 + \frac{(2.441 \times 10^7)}{(\lambda^2 - 0.803 \times 10^7)}$$

where, λ is the operating wavelength(μm) and C1 ≈ 5.446 μm^{-1}.

Confinement loss plays a vital role in determining the efficiency and accuracy of optical fiber sensors. It quantifies the amount of light attenuation while propagating through the core region of the PCF [53]. The equation for confinement loss can be expressed as follows [50]:

$$\text{Confinement loss} = 8.686x\frac{2\Pi}{\lambda}\text{x Im}(n_{\text{eff}})\text{x}10^4(\text{dB/cm}).$$

where Im (neff) - imaginary part of the effective mode index, λ- operating wavelength in μm.

In SPR-based sensing, sensitivity plays a crucial role in quantifying the change in the sensor's response caused by variations in the RI of the analyte. PCF-based SPR sensors demonstrate high sensitivity by confining light within the sensing layer, leading to a larger interaction area and enhanced responsiveness to RI changes. Variations in the RI of the analyte cause the resonance peak magnitude or wavelength of the sensor shifts accordingly, either to higher or lower values. The sensitivity of the sensor determines how well it performs, and this property may be evaluated in a number of different ways, including its sensitivity in terms of both amplitude and wavelength. The precise formula for calculating sensitivity based on wavelength is as follows [50],

$$s_\lambda = \frac{\Delta\lambda_{\text{Peak}}}{\Delta n_a}(\text{nm/RIU})$$

where, $\Delta\lambda_{peak}$ denotes the shift in peak wavelength, Δn_a denotes the change in the RI of the analyte.

The amplitude sensitivity of the sensor is determined using the following equation [50]:

$$s_a = -\frac{\Delta_a(\lambda, n_a)/\Delta n_a}{a(\lambda, n_a)}(\text{RIU}^{-1})$$

where $\Delta_a(\lambda, n_a)$ is the difference in the loss spectrum between adjacent analyte RI values, $a(\lambda, n_a)$ denotes the maximum overall loss and Δn_a denotes the change in the RI of the analyte.

Birefringence is a special property of light that helps differentiate between two polarization modes (X and Y modes) and their interactions with the analyte. This differentiation plays a crucial role in polarization control within PCF-based sensors, minimizing losses, crosstalk, and improving sensitivity [54], [55]. The numerical calculation of birefringence (B) of the proposed sensor is done using the following formula [56],

$$B = \left|\text{Re}\left(n_{eff}x\right) - \text{Re}\left(n_{eff}y\right)\right|$$

where, Re (n_{eff} x) and Re (n_{eff} y) are the real part of the effective RI in x and y polarization modes.

The resolution of the sensor determines its ability to detect tiny changes in the RI of the analyte. The following equation represents the measure of the minimum observable limit of RI [50]:

$$\text{Resolution} = \Delta n_{aX}\frac{\Delta\lambda_{min}}{\Delta\lambda_{Peak}}(\text{RIU})$$

$\Delta\lambda_{min}$ denotes the minimum spectral resolution, set at 0.1 nm. $\Delta\lambda_{peak}$ represents the peak wavelength shift, while Δn_a signifies the change in the RI of the analyte.

Another important parameter for evaluating the effectiveness of the sensor is the figure of merit (FOM). The FOM is determined by dividing the sensitivity (S_λ) by the full width at half maximum (FWHM). This value can be calculated using the following equation [50]:

$$\text{FOM} = \frac{s_\lambda(nm/RIU)}{FWHM(nm)}(\text{RIU}^{-1})$$

B. ELECTRIC FIELD DISTRIBUTION AND DISPERSION CHARACTERISTICS OF THE PROPOSED STRUCTURE

The electric field distribution of the proposed sensor is shown in Fig 2(a, b) for Ch1 and Ch2 respectively. In the proposed structure, light is incident at the air-core interface and guided within the core through the principle of MTIR. In Figs 2(a, b) (i, ii), the X and Y-polarized modes are depicted when

the incident light is guided through the core. When a phase matching condition is met, the optimum transfer of energy from the core mode to the plasmon mode occurs, which is referred to as coupling mode. This criterion ensures an efficient transfer of energy, resulting in enhanced performance of the sensor [57]. Figs 2(a, b) (iii, iv) illustrate the coupling mode and plasmon mode, respectively. These field distributions provide valuable insights for optimizing the sensor's design and performance.

Upon introducing the analyte into the structure, it induces a change in the effective RI of the structure. In PCF based SPR sensors, the resonance wavelength is a critical factor for detecting the analyte's RI. At this wavelength, the sensor experiences the highest peak of confinement loss, indicating the optimal coupling between the modes. Any variations in the analyte's RI have a direct impact on the sensor structure's effective RI. As a result, the sensor's resonance wavelength shifts either towards longer or shorter wavelengths. This wavelength shift method is widely employed to assess the sensor's sensitivity and evaluate its performance. Improving the coupling efficiency between core modes and the surrounding medium can enhance the sensor's sensitivity and its detection limit. Plasmon modes, on the other hand, generate strong localized electromagnetic fields at the metal-dielectric interface, which extend into the analyte medium, amplifying the interaction between analyte molecules and the evanescent field. This intensified interaction results in an enhanced detection limit and overall performance of the sensor.

The dispersion relation of the core guided mode of the proposed sensor is illustrated in Figs. 3 (a,b), depicting the variation with wavelength in the presence and absence of adhesive layers. In this study, two sensing channels, denoted as Ch1 and Ch2, are employed for simultaneous detection. Ch1's RI is fixed at 1.33, while Ch2's RI is set to 1.34. The real part of the effective index of the core guided mode decreases as the wavelength increases. In Fig. 3 (a), leaky modes start to emerge in the core mode at a wavelength of 1.35μm and couple with the plasmon mode in both Ch1 and Ch2. This coupling results in a slight decrease in the real part of the index, indicating the transfer of energy from the core mode to the plasmon mode. This phenomenon is known as phase matching, where the imaginary part of the effective index reaches its maximum value. Conversely, in Fig. 3 (b), the phase matching condition is achieved at 1.7μm for Ch1 and 1.5μm for Ch2, revealing the wavelength shift between the two channels. By comparing the coupling efficiencies of the X-polarized and Y-polarized modes, it is observed that the X-polarization exhibits superior coupling efficiency. Therefore, subsequent analysis focuses on the X-polarization.

III. RESULTS AND DISCUSSION

A. STRUCTURAL PARAMETER OPTIMIZATION

Achieving optimal sensor performance involves analyzing various structural parameters such as air hole diameter, pitch size, plasmon layer thickness, sensing channel thickness, and the gap between the two sensing channels. By assessing the impact of these parameters, the sensor's sensitivity and overall efficiency can be optimized. This can be done by individually varying these parameters while keeping other structural factors constant, allowing for the evaluation of their impact on confinement loss at different wavelengths. In order to maintain consistency with the analyte RI, the optimization process includes maintaining a constant RI value of 1.33 for Ch1 and 1.34 for Ch2, which falls within the range of blood plasma RIs for TB patients [3]. Through meticulous parameter optimization, significant improvements can be achieved in the sensor's performance.

1) OPTIMIZATION OF PLASMONIC LAYER THICKNESS

The effectiveness of SPR based PCF sensors is highly sensitive to the plasmonic layer thickness; hence, optimization efforts began with the metal layers themselves [58]. Two different metallic layers such as gold and silver are utilized for different channels. Two different metallic layers cause variations in the evanescent field during plasmon wave generation, resulting in distinct resonance wavelengths for gold and silver metals [58]. The gold is used as the plasmonic metal for Ch1 to induce the plasmonic effect. The ideal thickness of the gold layer is being determined by varying the t_{Au} values of 0.03 μm, 0.04 μm, and 0.05 μm. Fig. 4(a) illustrates the confinement loss spectra of the proposed structure as the t_{Au} is gradually increased. The results demonstrate that as the t_{Au} increases, the resonance wavelength shifts towards longer wavelengths, and there is an increase in the coupling efficiency between the core mode and plasmon mode up to 0.04 μm. However, beyond this thickness, the coupling efficiency starts to decrease due to the increased damping loss resulting from the thicker gold layer [59]. Therefore, the optimal value for achieving strong coupling efficiency is determined to be 0.04 μm for the gold layer thickness. In Ch1, the graphene layer is introduced over the gold layer to act as a catalyst, enhancing the effectiveness of the sensor. Graphene's notable optical characteristics, rapid electron mobility, and expansive specific surface area facilitate biomolecule absorption, leading to enhanced sensitivity in biomolecule detection [60]. The ideal thickness of the graphene layer is determined by varying the $t_{graphene}$ values of 0.008 μm, 0.01 μm, and 0.012 μm while maintaining t_{Au} at 0.04 μm. Fig. 4(b) showcases the confinement loss spectra of the proposed structure as $t_{graphene}$ is gradually increased. Similar to t_{Au}, as the thickness ($t_{graphene}$) increases, the resonance wavelength shifts towards longer wavelengths. Moreover, an increase in the coupling efficiency between the core mode and plasmon mode is observed up to a thickness of 0.01 μm. However, beyond this value, the coupling efficiency begins to decrease. Consequently, the optimal thickness for achieving strong coupling efficiency is determined to be 0.01 μm for the graphene layer.

In Ch2, silver is employed as the plasmonic material. Fig. 4(a) displays the confinement loss spectra for different t_{Ag} values of 0.03 μm, 0.04 μm, and 0.05 μm. A thickness

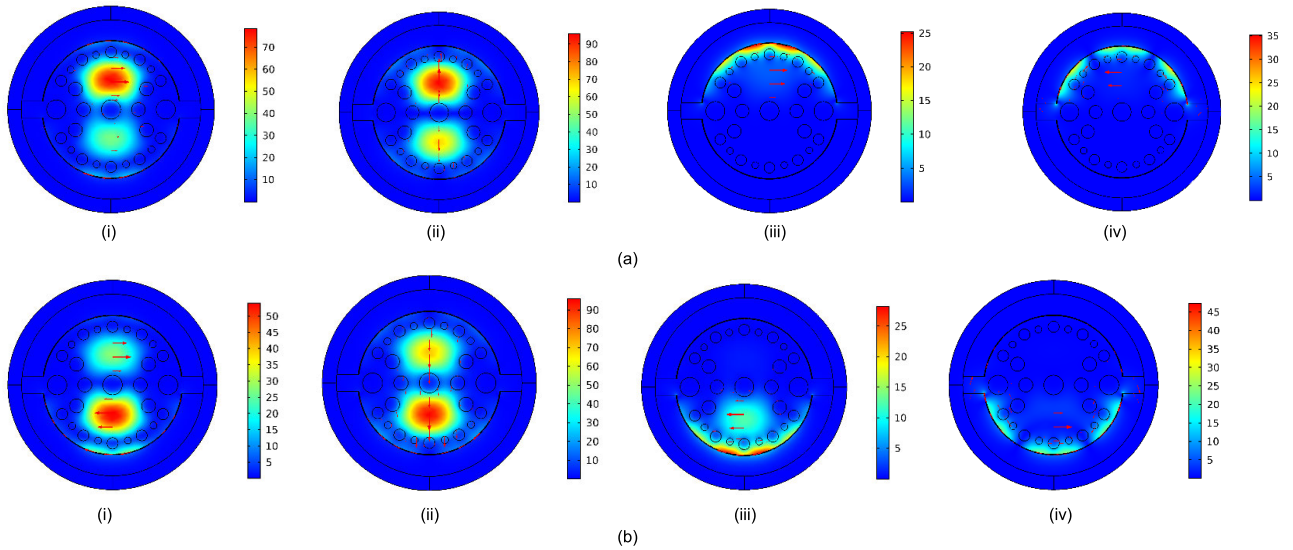

FIGURE 2. Distribution of electric field for the proposed dual-channel PCF based SPR sensor: (i) X-polarized mode, (ii) Y- polarized mode, (iii) coupling mode, (iv) plasmon mode in (a) Ch1 and (b) Ch2.

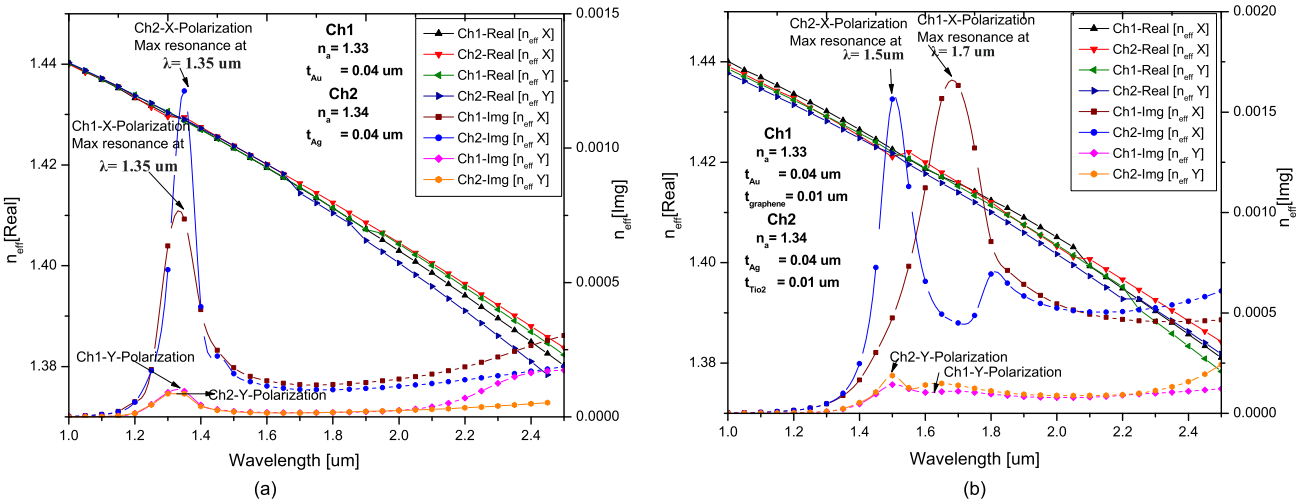

FIGURE 3. Dispersion characteristics of the proposed sensor as a function of wavelength: (a) without adhesive layer; (b) with adhesive layer.

of 0.04 μm is determined to be the ideal value, similar to gold, for achieving better coupling efficiency. Additionally, TiO_2 is used as an adhesive layer in order to enhance sensor performance and prevent oxidation of the plasmonic metal. Fig. 4(b) illustrates the confinement loss spectra as t_{TiO2} is varied with thickness values of 0.008 μm, 0.01 μm, and 0.012 μm. Similar to Ch1, a thickness of 0.01 μm is found to be the optimal thickness of TiO_2 for improved sensor performance.

2) OPTIMIZATION OF SENSING CHANNEL THICKNESS

The sensing channel thickness ($t_{sensing\ channels}$) plays a crucial role in tuning SPR-based PCF sensors. In the proposed structure, two sensing channels, namely Ch1 and Ch2, are utilized. Fig. 5(a) illustrates the confinement loss spectra for different values of the sensing channel thickness, specifically 1 μm, 1.5 μm, and 2 μm. The results indicate that as the sensing channel thickness increases, the resonance depth in the loss spectra also increases. This suggests a stronger coupling between the core mode and plasmon mode, facilitated by a reduced distance between the core and plasmon layer when the sensing channel thickness expands. However, $t_{sensing\ channels}$ exceeding 1.5 μm causes the loss spectrum to broaden, thereby reducing the sensor's sensing efficiency. Conversely, increasing the sensing channel thickness brings the core and metal surface closer together, significantly enhancing the coupling efficiency between the core and plasmon modes. This leads to interference effects and the distinctive emergence of a second resonance peak in the sensor response. Based on these findings, a sensing channel thickness of 1.5 μm is chosen as the optimal thickness to enhance the sensor's performance.

3) OPTIMIZATION OF INTER CHANNEL GAP

The inter-channel gap is an additional tuning parameter in SPR-based PCF sensors. By varying the distance between the

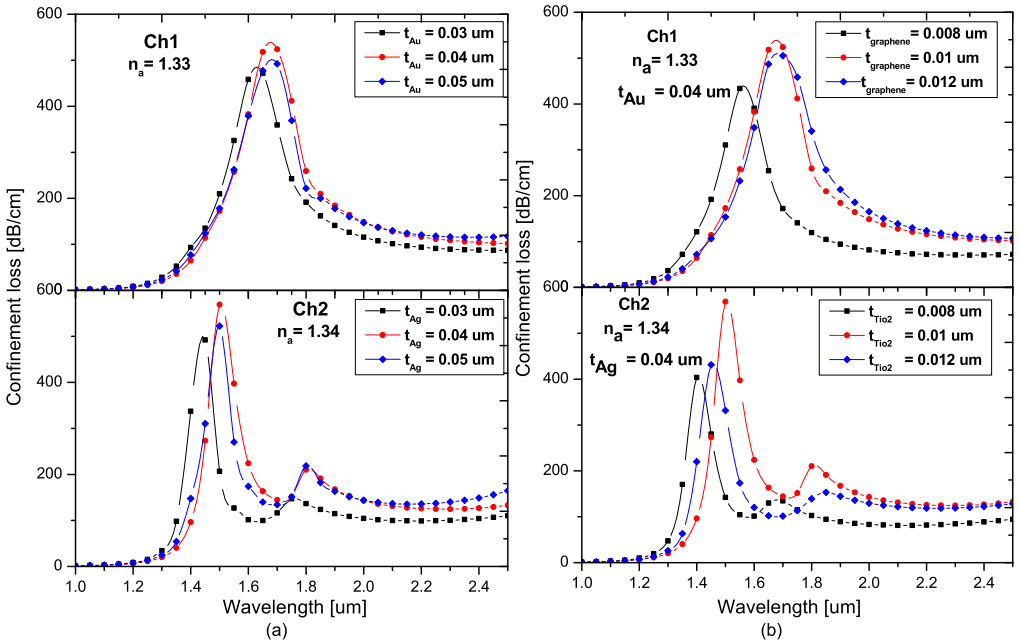

FIGURE 4. Loss spectrum for (a) variations in t_{Au} and t_{Ag}; (b) variations in $t_{graphene}$ and $tTiO_2$ for Ch1 and Ch2 as a function of wavelength.

two channels at values of 0.08 μm, 0.1 μm, and 0.12 μm while keeping other parameters constant, the ideal gap can be determined. The findings reveal that as the inter-channel gap increases, the resonance depth in the loss spectra decreases. This is because when the two channels are closely positioned, the resonance becomes hybridized [61]. Among the tested gaps, a gap size of 0.1 μm exhibits a highly sharp resonance in the loss spectrum. Therefore, this value is considered the optimal choice for analyzing the sensor's performance. Fig. 5(b) depicts the confinement loss spectra for different values of the inter channel gap.

4) OPTIMIZATION OF AIR HOLE DIAMETER

The size of the airholes significantly impacts the sensor's detection capabilities as they establish the path between the core and the analyte. When airholes are smaller, they create a broader pathway between the core mode and plasmon mode, resulting in increased confinement loss due to light leakage. Enhancing the coupling efficiency between the core guided mode and plasmon mode involves deliberately reducing the size of the coupling air hole. The optimization process includes considering values of coupling air hole diameter (d4) such as 0.4μm, 0.5μm, and 0.6μm. Fig. 5(c) depicts the confinement loss spectra for different diameter values of air hole as a function of wavelength for Ch1 and Ch2. The results indicate that as the diameter of the coupling airhole increases i.e. 0.6 μm, the loss spectrum decreases, and peak shifting occurs towards shorter wavelengths. Conversely, a smaller diameter of 0.4μm provides a broader spectrum to due to the larger path between the core mode and plasmonic mode. A 0.5μm diameter airhole restricts the path between the core guided mode and plasmon mode, resulting in reduced coupling efficiency. Among the different diameters, a diameter of 0.5 μm exhibits a highly sharp resonance in the loss spectrum, making it the optimal choice for analyzing the sensor's performance.

5) OPTIMIZATION OF PML THICKNESS

The PML layer reduces light reflection and scattering losses at the PCF boundary. Increasing its percentage improves phase matching, leading to reduced reflection losses and enhanced PCF performance. When the PML layer's thickness (t_{PML}) ranges from 5% to 10% of the PCF diameter, it enables better mode matching and reduces reflection losses at the boundary [62]. The analysis considers PML thicknesses of 0.5 μm, 1 μm, and 1.5 μm. The findings, shown in Fig. 5(d) for Ch1 and Ch2, clearly demonstrate that a thickness of 1 μm provides tight confinement, enhancing phase matching and resulting in higher confinement loss. These results suggest that using a PML layer with a thickness of 1 μm can offer advantages in achieving improved mode matching and minimizing reflection losses, particularly in sensing applications.

The optimized sensor structure introduces birefringence in two ways: by creating asymmetry in the cladding region through the use of four different sizes of air holes, and by utilizing different plasmonic materials, gold and silver, for Ch1 and Ch2, respectively. This approach achieves a birefringence value of 1.40 X 10^{-3} for Ch1 and 2.05 X 10^{-3} for Ch2. The significant birefringence enhances the sensitivity of the sensor, making it more capable of detecting and measuring changes in the analyte.

B. EVALUATING SENSOR PERFORMANCE

The detection mechanism of a SPR based PCF sensor relies on the degree of coupling between the plasmon mode and the core mode. This coupling is influenced by fundamental

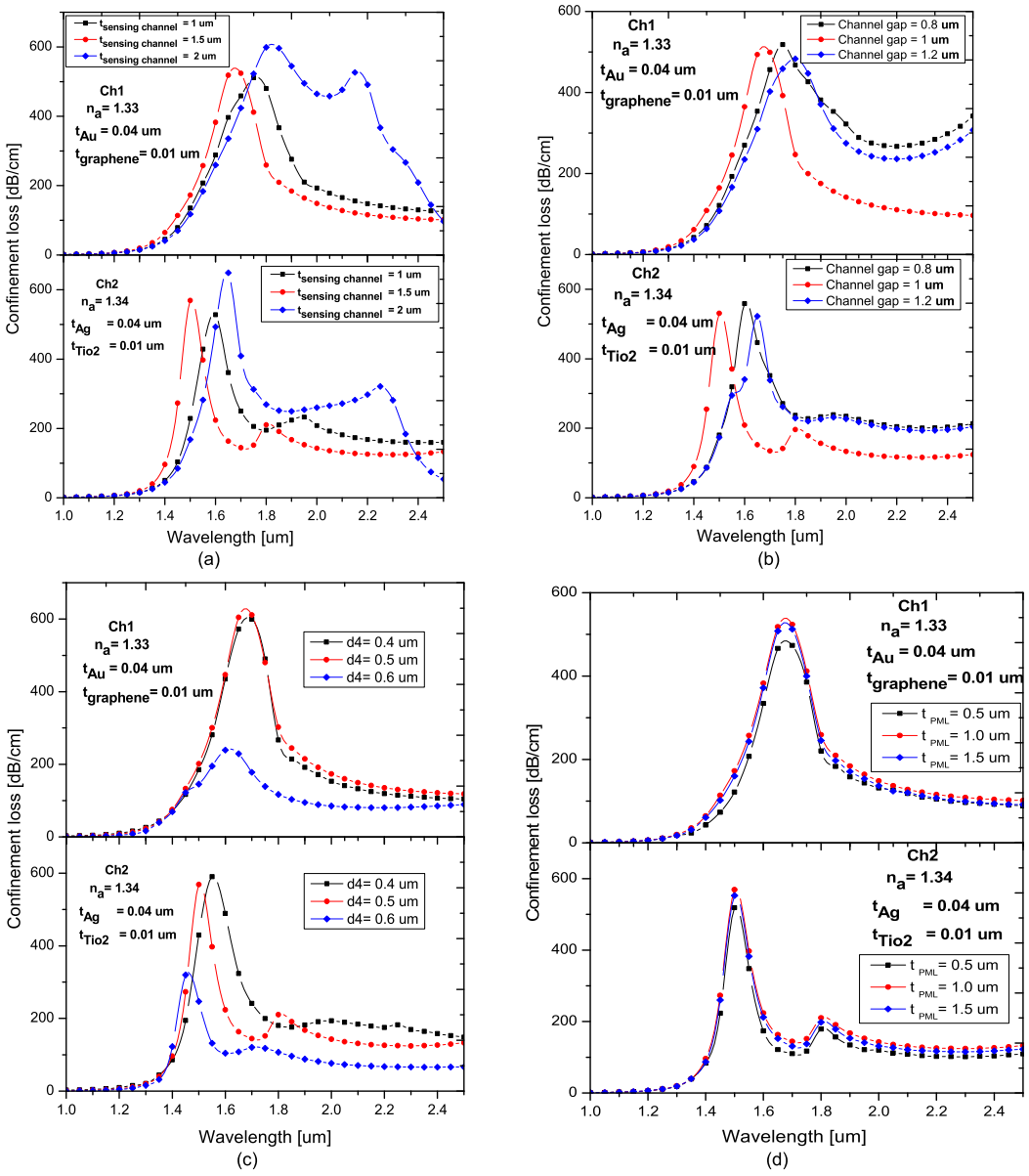

FIGURE 5. Loss spectrum for (a) different sensing channel thickness; (b) different inter channel gap; (c)different air hole diameter; (d) different PML thickness for Ch1 and Ch2.

characteristics such as confinement loss and resonance wavelength, which play a crucial role in detecting and identifying an unknown analyte. The resonance properties of the sensor are impacted by changes in the RI of the analyte. This can be observed as either a change in the magnitude of the resonance peak or a shift in the resonance wavelength to a higher or lower value. These changes in the SPR signal provide valuable information about the analyte's RI and can be used for detecting and identifying the unknown analyte. In SPR sensing, wavelength sensitivity is a significant parameter that measures the change in resonance wavelength due to variations in the RI of the analyte. PCF-based SPR sensors offer high sensitivity because they can confine light within the sensing layer, resulting in a greater interaction area and improved sensitivity to RI changes.

The performance of the proposed sensor is being evaluated for biosensing applications by filling the sensing channels with biological samples. The sensor incorporates a dual-channels to simultaneously detect two distinct biological indicators. Blood and urine are the initial indicators of any illness in the human body. Consequently, the sensor utilizes blood samples infected with Mycobacterium tuberculosis [2], [3] and urine samples infected with both gram-positive and gram-negative bacteria as analytes [63], [64], [65]. These biological samples facilitate the concurrent detection of TB and UTIs.

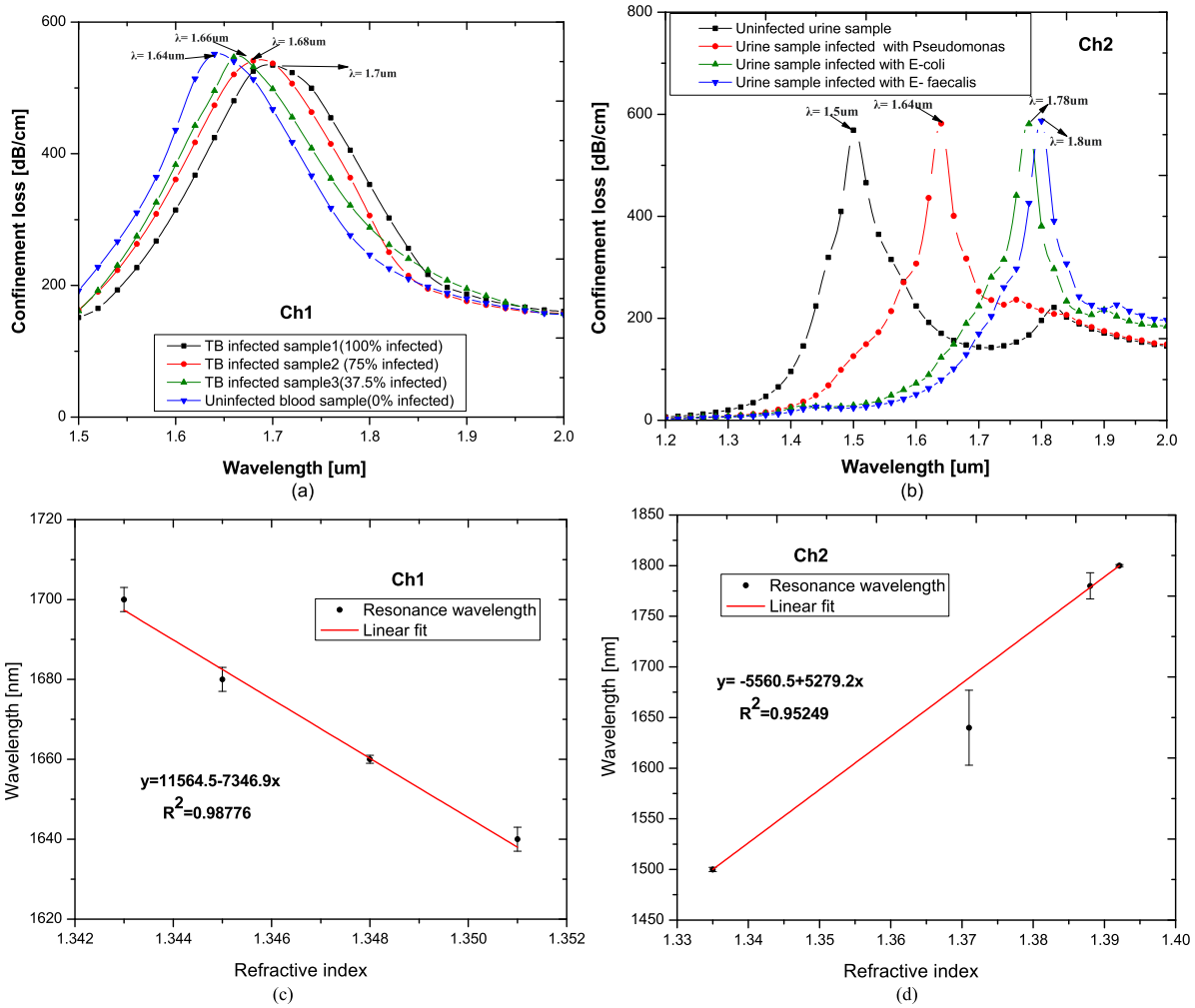

FIGURE 6. Loss spectra of Ch1and Ch2 for (a) bacteriomes causing TB; (b) bacteriomes causing UTI with respect to wavelength; Linear fitting and error bars between the refractive index of different analytes and resonance wavelength for (c) TB detection; (d) UTI detection.

During the preliminary evaluation, Ch1 is considered to be filled with blood samples, which encompass both uninfected blood samples and different levels of infected samples from TB patients, each exhibiting different refractive indices. These blood samples could be prepared, with a volume of 5 ml, are intended to be collected with EDTA (Ethylenediaminetetraacetic acid) anticoagulant and stored at 4°C until use. experimental procedures are carried out within three hours of collection to preserve sample integrity. Plasma is separated from the blood through centrifugation at 1500 rpm for approximately 15 minutes [66]. Subsequently, equal amounts of plasma and red blood cells are combined, with efforts made to maintain a constant hematocrit level. Each of these samples exhibits different refractive indices. The coupling response of a known uninfected blood sample (0% severity) with a RI of 1.351 [3] is initially assessed, and this resonance wavelength becomes the reference wavelength for subsequent analyses. Deviations in RI arise due to contamination with Mycobacterium tuberculosis bacteria, leading to RI variations. To detect TB infection, three distinct infected samples with refractive indices of 1.343 (100% severity), 1.345 (75% severity), and 1.348 (37.5% severity) are employed [3]. The initial analysis reveals that Ch1 exhibits a resonance wavelength of 1.64 μm at a RI of 1.351. Using this resonance wavelength as the reference, deviations from this value indicate the severity of the infection. This phenomenon is prominently displayed in the confinement loss spectra illustrated in Fig. 6(a). Notably, as the infection rate increases, the confinement loss peak shifts towards longer wavelengths. Samples with an RI of 1.343 exhibit a greater deviation from the reference wavelength, indicating a higher degree of infection impact, while samples with an RI of 1.348 display a smaller deviation, suggesting milder infections. Ch1 achieves a maximum wavelength sensitivity of 10,000 nm/RIU within this context.

Concurrently, Ch2 is investigated using a different set of urine samples, including both infected and uninfected instances, with the objective of detecting UTIs and identifying the specific pathogen responsible. The response of an established uninfected urine sample with a RI of 1.335

TABLE 1. Evaluation of the proposed sensor performance with biological samples.

Channel	Analyte / severity (%)	Refractive index (n)	Resonance wavelength (nm)	Wavelength difference (nm)	Wavelength sensitivity (nm/RIU)	Resolution (RIU)	FOM [RIU^{-1}]
Ch1	TB infected sample 1 / 100%	1.343	1700	-	-	$1x10^{-5}$	-
	TB infected sample 2 / 75%	1.345	1680	20	10000	$1.5x10^{-5}$	1000
	TB infected sample 3/ 37.5%	1.348	1660	20	6666.67	$1.5x10^{-5}$	740.74
	Uninfected blood sample / 0%	1.351	1640	20	6666.67	-	833.33
Ch2	Uninfected urine sample / 0%	1.335	1500	-	-	$2.57x10^{-5}$	-
	UTI infected sample 1 / 63%	1.371	1640	140	3888.88	$1.5x10^{-5}$	972.22
	UTI infected sample 2 / 92.8%	1.388	1780	140	8235.29	$1.21x10^{-5}$	1647.04
	UTI infected sample 3/ 100%	1.3921	1800	20	5000	-	1666.67

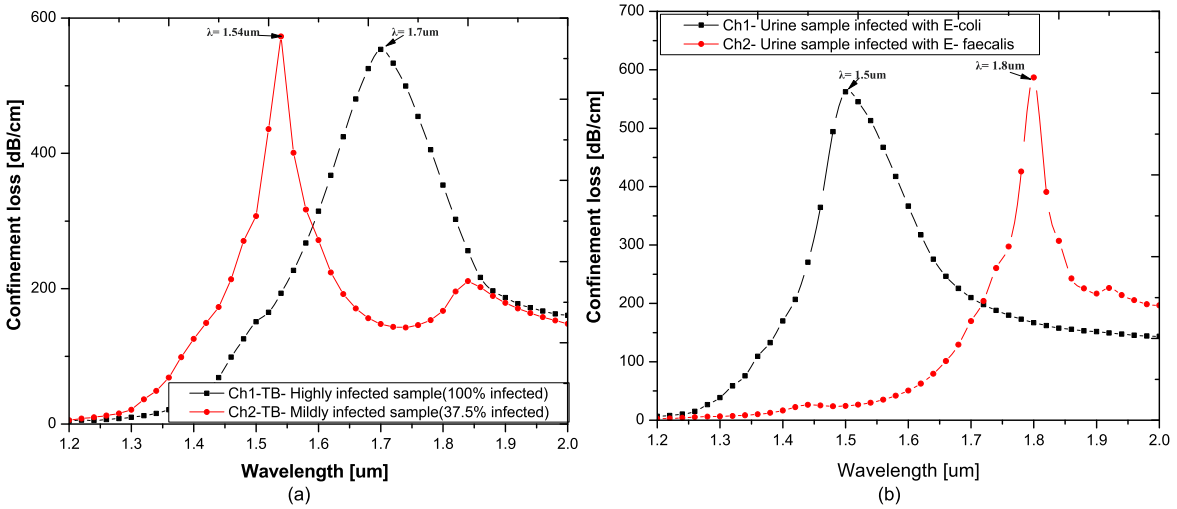

FIGURE 7. Loss spectra between Ch1and Ch2 for (a) bacteriomes causing TB; (b) bacteriomes causing UTI with respect to wavelength.

TABLE 2. Evaluation of the proposed sensor performance with biological samples between Ch1 and Ch2.

Analyte	Channel	Refractive index (n)	Resonance wavelength (nm)	Confinement loss (dB/cm)	Wavelength sensitivity (nm/RIU)	Resolution (RIU)
bacteriomes causing TB	Ch1 (Highly infected)	1.343	1700	553.41	32000	$3.33x10^{-6}$
	Ch2 (Mildly infected)	1.348	1540	572.10		
bacteriomes causing UTI	Ch1 (E-Coli)	1.388	1500	562.28	73170	$1.37x10^{-6}$
	Ch2 (E-Faecalis)	1.3921	1800	586.83		

[63] is initially evaluated, and this particular resonance wavelength is adopted as the reference point for subsequent analyses. The RI of infected samples varies depending on the specific pathogen causing the infection. Differential staining techniques are employed to differentiate between gram-positive (E. faecalis) and gram- negative (E. coli and Pseudomonas) bacteria. For UTI detection, three separate samples infected with distinct pathogens, featuring refractive indices of 1.371 for Pseudomonas, 1.388 for E. coli, and 1.3921 for Faecalis [64], [65] are employed. In Ch2, a resonance wavelength of 1.5 μm is observed for an RI of 1.335, representing the resonance behavior of uninfected urine samples. Utilizing this established resonance wavelength as a reference point, deviations from this value offer valuable insights into the specific type of pathogen infecting the respective sample. This phenomenon is prominently illustrated in the confinement loss spectra shown in Fig. 6(b). Any deviations from the reference wavelength indicate the presence of specific types of pathogen infections within the samples. The confinement loss spectra in Fig. 6(b) visually depict this behavior, where the peak shifts towards longer wavelengths as the RI of the analyte increases. Ch2 demonstrates an optimal wavelength sensitivity of 8235.29nm/RIU. Furthermore, an extensive performance analysis of both

TABLE 3. Analysis of the proposed biosensor in comparison with recently reported studies.

Reference	Structure / Materials used	Application		Wavelength sensitivity (nm/RIU)	Resolution (RIU)	Detection range	Resonant Wavelength range (nm)	Nature of Results
A. Yasli et.al., 2021 [67]	SPR based PCF biosensor / Gold	Cancer detection		7142.86	$1.4x10^{-5}$	1.392 – 1.401	730 - 850	Numerical study
V. S. Chaudhary et. al., 2021 [23]	PCF based SPR biosensor/ Gold	Malaria parasite detection		14285.71	-	1.373 – 1.402	836-936	Numerical study
M. Aliee et.al., 2022 [25]	PCF based SPR biosensor/ Gold	Coronavirus detection		1172	-	1.395 – 1.435	482-532	Numerical study
M. E. Rahaman et. al., 2022 [39]	PCF based SPR biosensor/ Gold	Glucose level detection		2500	$4 x10^{-6}$	1.338 – 1.358	630 -660	Numerical study
V. S. Chaudhary et. al., 2022 [24]	PCF based SPR biosensor/ Gold- Tio_2	blood compositions detection		12400	$8.06 x10^{-6}$	1.33 – 1.40	784 - 1032	Numerical study
P. Manickam et.al., 2022 [68]	Side polished PCF based SPR sensor / Silver-MgF_2	Urine analysis		20000	$5 x10^{-7}$	1.337 – 1.342	1050 -1150	Numerical study
M. Abdelghaffar et. al., 2023 [69]	V shaped SPR based PCF biosensor / ZrN	Cancer detection		6214.28	$2.782 x10^{-5}$	n_a= 1.385 n_b= 1.399	688-765	Numerical study
P. Manickam et.al., 2023 [70]	PCF based SPR biosensor/ Gold-GeO_2	Urinary Methanol detection		5000	$1 x10^{-5}$	1.33 – 1.36	1260 - 1120	Numerical study
Proposed sensor	Dual-channel PCF based SPR sensor / Gold-graphene / Silver-TiO_2	Tuberculosis detection	Ch1	10000	$1x10^{-5}$	1.343-1.351	1700 - 1540	Numerical study
			Between Ch1 and Ch2	32000	$3.33x10^{-6}$	n_a= 1.343 n_b= 1.348		
		Urinary tract infection detection	Ch2	8235.29	$1.21x10^{-5}$	1.335-1.3921	1500 - 1800	Numerical study
			Between Ch1 and Ch2	73170	$1.37x10^{-6}$	n_a= 1.388 n_b= 1.3921		

Ch1 and Ch2 is presented in Table 1 of the proposed biosensor.

Fig. 6 (c, d) illustrates the linear fitting and error bars of resonance wavelength as a function of analyte's RI for TB and UTI detection, respectively. The slope of these equations, as mentioned in Fig. 6 (c, d), indicates the average sensitivity across various RI values. In particular, the sensitivities are 11564.5 nm/RIU for TB detection for the RI range of 1.343 to 1.351 and 5560.5 nm/RIU for UTI detection for the RI range of 1.335 to 1.3921. The fitted lines display remarkable linearity with R2 values of 0.98776 and 0.95249 for TB and UTI detection, respectively, indicating a highly linear sensing response in the proposed sensor structure. The error bars represent the maximum measured deviations.

In the prior analysis, Ch1 is intentionally utilized for TB detection, while Ch2 is allocated for UTI detection. However, the proposed dual-channel sensor can detect distinct infected samples of the same disease. In the ongoing evaluation phase, the different samples of same dieses are used as an analyte for both Ch1 and Ch2. In assessing the sensor's efficacy, Ch1 is loaded with a highly infected blood sample (100%) possessing a RI of 1.343. Conversely, Ch2 contains a mildly infected blood sample (37.5%) with an RI of 1.348, as identified in the preceding analysis. Fig. 7(a) depicts the confinement loss spectra, which represent the behavior of highly and mildly infected blood at different wavelengths. In these spectra, Ch1 displayed its highest resonance peak at 1.7 μm, whereas Ch2 exhibited its maximum resonance peak at 1.54 μm. At the resonance of 1.7 μm, Ch1 showed a peak confinement loss of 553.41 dB/cm, whereas Ch2 demonstrated a peak confinement loss of 572.10 dB/cm at the resonance point of 1.54 μm. The sensor demonstrated their greatest sensitivity between Ch1 and Ch2, with a value of 32,000 nm/RIU.

Likewise, urine samples infected with both gram-positive bacteria (E. faecalis) and gram-negative bacteria (E. coli) are employed as a biological indicator to detect UTIs. In evaluating the sensor's performance, Ch1 is being filled with an E. coli bacteria-infected sample, and Ch2 contains an E. faecalis bacteria-infected sample. Fig. 7(b) presents the confinement loss spectra of the proposed sensor for both bacteria types across various wavelengths. In these confinement loss spectra, Ch1 displays its primary resonance point at 1.5 μm, while Ch2 demonstrates its highest resonance peak at 1.8 μm. At the 1.5 μm resonance point, Ch1 registers a peak confinement loss of 562.28 dB/cm, whereas Ch2 records a peak confinement loss of 586.83 dB/cm at the 1.8 μm resonance point. The channels exhibited their highest wavelength sensitivity between Ch1 and Ch2, reaching a value of 73,170 nm/RIU. A comprehensive performance analysis of both Ch1 and Ch2 is presented in Table 2 of the proposed biosensor. The enhanced sensitivity is attributed to the use of two distinct plasmonic materials within the dual-channel structure, resulting in improved sensitivity and reduced cross-coupling effects.

When compared to the latest research findings, the proposed sensor demonstrates significantly superior performance. This performance comparison is presented in Table 3, and the analysis assesses the sensor's ability to detect two distinct diseases, TB and UTI, in both single-channel detection and between two channels. It becomes evident that our

proposed sensor outperforms existing sensors significantly in terms of its performance capabilities.

IV. CONCLUSION

In conclusion, the proposed dual-channel PCF-based SPR biosensor offers a highly sensitive solution for simultaneous detection of two different analytes. The proposed sensor contains two channels to demonstrates simultaneous detection of two different substances, ensuring efficient and precise analysis. Ch1 utilizes a 0.04μm-thick layer of gold, and Ch2 employs a silver layer of the same thickness as plasmonic materials to induce the SPR effect. To further enhance sensor performance, a graphene layer of 0.01μm thickness is coated with gold in Ch1, and a same thickness TiO_2 layer is coated over the silver in Ch2. These enhancements lead to distinct resonance peaks at varying wavelengths, dependent on the RI of the analyte. Through numerical investigations using the FEM, the sensor's performance has been evaluated and optimized.

The effectiveness of the proposed sensor is assessed for biosensing applications through the introduction of biological samples into the sensing channels. For this evaluation, RI data from the literature related to diseases like TB and UTIs are utilized. In the case of TB detection, the RI value of blood samples infected with Mycobacterium tuberculosis is employed. For UTI detection, urine samples infected with both gram-positive and gram-negative bacteria are used, facilitating early diagnosis. Ch 1 primarily focuses on TB detection, while Ch 2 is dedicated to UTI detection. This dual-channel approach demonstrates impressive maximum wavelength sensitivities, with 10,000 nm/RIU for TB detection and 8,235.29 nm/RIU for UTI detection. The biosensor's versatility is demonstrated through its successful detection of various samples of the same diseases. It effectively distinguishes between highly and mildly infected blood samples in TB detection and discriminates different bacterial infections in UTI detection. The analysis reveals remarkable maximum sensitivities of 32,000 nm/RIU with a sensing resolution of 3.33×10^{-6} RIU for TB detection and 73,170 nm/RIU with a sensing resolution of 1.37×10^{-6} RIU for UTI detection. The proposed biosensor provides a reliable platform for disease monitoring, featuring heightened sensitivity and a broad detection range. Its applications extend beyond medical diagnostics to encompass biochemical sensing, drug discovery and development, as well as ensuring food safety

ACKNOWLEDGMENT

The authors thank VIT for providing ''VIT RGEMS SEED GRANT'' for carrying out this research work.

REFERENCES

[1] D. Dhamnetiya, P. Patel, R. P. Jha, N. Shri, M. Singh, and K. Bhattacharyya, ''Trends in incidence and mortality of tuberculosis in India over past three decades: A joinpoint and age–period–cohort analysis,'' *BMC Pulmonary Med.*, vol. 21, no. 1, pp. 1–14, Dec. 2021, doi: 10.1186/s12890-021-01740-y.

[2] N. A. Mohammed, O. E. Khedr, E.-S.-M. El-Rabaie, and A. A. M. Khalaf, ''High-sensitivity early detection biomedical sensor for tuberculosis with low losses in the terahertz regime based on photonic crystal fiber technology,'' *Photonic Sensors*, vol. 13, no. 2, pp. 1–16, Jun. 2023, doi: 10.1007/s13320-023-0675-z.

[3] J. Parmar, S. K. Patel, V. Katkar, and A. Natesan, ''Graphene-based refractive index sensor using machine learning for detection of mycobacterium tuberculosis bacteria,'' *IEEE Trans. Nanobiosci.*, vol. 22, no. 1, pp. 92–98, Jan. 2023, doi: 10.1109/TNB.2022.3155264.

[4] J. Chakaya, E. Petersen, R. Nantanda, B. N. Mungai, G. B. Migliori, F. Amanullah, P. Lungu, F. Ntoumi, N. Kumarasamy, M. Maeurer, and A. Zumla, ''The WHO global tuberculosis 2021 report—Not so good news and turning the tide back to end TB,'' *Int. J. Infectious Diseases*, vol. 124, pp. S26–S29, Nov. 2022, doi: 10.1016/j.ijid.2022.03.011.

[5] S. Al Abri et al., ''Tools to implement the world health organization end TB strategy: Addressing common challenges in high and low endemic countries,'' *Int. J. Infectious Diseases*, vol. 92, pp. S60–S68, Mar. 2020, doi: 10.1016/j.ijid.2020.02.042.

[6] B. Kaur, S. Kumar, and B. K. Kaushik, ''Antimonene, CNT and MoS_2 based SPR-fiber-optic probe for tuberculosis detection,'' *IEEE Sensors J.*, vol. 22, no. 15, pp. 14903–14910, Aug. 2022, doi: 10.1109/JSEN.2022.3186995.

[7] M. Trzaskowski, A. Napiórkowska, E. Augustynowicz-Kopeć, and T. Ciach, ''Detection of tuberculosis in patients with the use of portable SPR device,'' *Sensors Actuators B, Chem.*, vol. 260, pp. 786–792, May 2018, doi: 10.1016/j.snb.2017.12.183.

[8] Z. Zeng, J. Zhan, and H. Chen, ''Global, regional, and national burden of urinary tract infections from 1990–2019: An analysis of the global burden of disease study 2019,'' *World J. Urol.*, vol. 40, no. 3, pp. 755–763, 2022, doi: 10.21203/rs.3.rs-829349/v1.

[9] E. Özgür, A. A. Topçu, E. Yılmaz, and A. Denizli, ''Surface plasmon resonance based biomimetic sensor for urinary tract infections,'' *Talanta*, vol. 212, May 2020, Art. no. 120778, doi: 10.1016/j.talanta.2020.120778.

[10] S. D. Gür, M. Bakhshpour, and A. Denizli, ''Selective detection of *Escherichia coli* caused UTIs with surface imprinted plasmonic nanoscale sensor,'' *Mater. Sci. Eng. C*, vol. 104, Nov. 2019, Art. no. 109869, doi: 10.1016/j.msec.2019.109869.

[11] J. Gomez-Cruz, S. Nair, A. Manjarrez-Hernandez, S. Gavilanes-Parra, G. Ascanio, and C. Escobedo, ''Cost-effective flow-through nanohole array-based biosensing platform for the label-free detection of uropathogenic E. coli in real time,'' *Biosensors Bioelectron.*, vol. 106, pp. 105–110, May 2018, doi: 10.1016/j.bios.2018.01.055.

[12] J. Jayalakshmi and V. Jayaram, ''Evaluation of various screening tests to detect asymptomatic bacteriuria in pregnant women,'' *Indian J. Pathol. Microbiol.*, vol. 51, no. 3, pp. 379–381, 2008.

[13] S. Kant, A. Lohiya, A. Kapil, and S. K. Gupta, ''Urinary tract infection among pregnant women at a secondary level hospital in Northern India,'' *Indian J. Public Health*, vol. 61, no. 2, pp. 118–123, 2017, doi: 10.4103/ijph.IJPH_293_15.

[14] J. Schnarr and F. Smaill, ''Asymptomatic bacteriuria and symptomatic urinary tract infections in pregnancy,'' *Eur. J. Clin. Invest.*, vol. 38, no. s2, pp. 50–57, Oct. 2008, doi: 10.1111/j.1365-2362.2008.02009.x.

[15] A. E. Barber, J. P. Norton, A. M. Spivak, and M. A. Mulvey, ''Urinary tract infections: Current and emerging management strategies,'' *Clin. Infectious Diseases*, vol. 57, no. 5, pp. 719–724, Sep. 2013, doi: 10.1093/cid/cit284.

[16] M. S. Kumar and A. P. Das, ''Emerging nanotechnology based strategies for diagnosis and therapeutics of urinary tract infections: A review,'' *Adv. Colloid Interface Sci.*, vol. 249, pp. 53–65, Nov. 2017, doi: 10.1016/j.cis.2017.06.010.

[17] M. A. C. Broeren, S. Bahçeci, H. L. Vader, and N. L. A. Arents, ''Screening for urinary tract infection with the Sysmex UF-1000i urine flow cytometer,'' *J. Clin. Microbiol.*, vol. 49, no. 3, pp. 1025–1029, Mar. 2011, doi: 10.1128/jcm.01669-10.

[18] M. S. Kumar, S. Ghosh, S. Nayak, and A. P. Das, ''Recent advances in biosensor based diagnosis of urinary tract infection,'' *Biosensors Bioelectron.*, vol. 80, pp. 497–510, Jun. 2016, doi: 10.1016/j.bios.2016.02.023.

[19] S. Nair, J. Gomez-Cruz, Á. Manjarrez-Hernandez, G. Ascanio, R. Sabat, and C. Escobedo, ''Selective uropathogenic E. coli detection using crossed surface-relief gratings,'' *Sensors*, vol. 18, no. 11, p. 3634, Oct. 2018, doi: 10.3390/s18113634.

[20] K. E. Mach, P. K. Wong, and J. C. Liao, ''Biosensor diagnosis of urinary tract infections: A path to better treatment?'' *Trends Pharmacol. Sci.*, vol. 32, no. 6, pp. 330–336, Jun. 2011, doi: 10.1016/j.tips.2011.03.001.

[21] H. Nguyen, J. Park, S. Kang, and M. Kim, "Surface plasmon resonance: A versatile technique for biosensor applications," *Sensors*, vol. 15, no. 5, pp. 10481–10510, May 2015, doi: 10.3390/s150510481.

[22] I. Pockrand, J. D. Swalen, J. G. Gordon, and M. R. Philpott, "Surface plasmon spectroscopy of organic monolayer assemblies," *Surf. Sci.*, vol. 74, no. 1, pp. 237–244, May 1978, doi: 10.1016/0039-6028(78)90283-2.

[23] V. S. Chaudhary, D. Kumar, and S. Kumar, "Gold-immobilized photonic crystal fiber-based SPR biosensor for detection of malaria disease in human body," *IEEE Sensors J.*, vol. 21, no. 16, pp. 17800–17807, Aug. 2021, doi: 10.1109/JSEN.2021.3085829.

[24] V. S. Chaudhary, D. Kumar, G. P. Mishra, S. Sharma, and S. Kumar, "Plasmonic biosensor with gold and titanium dioxide immobilized on photonic crystal fiber for blood composition detection," *IEEE Sensors J.*, vol. 22, no. 9, pp. 8474–8481, May 2022, doi: 10.1109/JSEN.2022.3160482.

[25] M. Aliee and M. H. Mozaffari, "Photonic quasi-crystal fiber-based plasmonic biosensor: A platform for detection of coronavirus," *Plasmonics*, vol. 17, no. 4, pp. 1655–1660, Aug. 2022, doi: 10.1007/s11468-022-01651-6.

[26] L. Li, Y.-N. Zhang, W. Zheng, X. Li, and Y. Zhao, "Optical fiber SPR biosensor based on gold nanoparticle amplification for DNA hybridization detection," *Talanta*, vol. 247, Sep. 2022, Art. no. 123599, doi: 10.1016/j.talanta.2022.123599.

[27] A. K. Sharma, A. K. Pandey, and B. Kaur, "A review of advancements (2007–2017) in plasmonics-based optical fiber sensors," *Opt. Fiber Technol.*, vol. 43, pp. 20–34, Jul. 2018, doi: 10.1016/j.yofte.2018.03.008.

[28] P. Falkowski, Z. Lukaszewski, and E. Gorodkiewicz, "Potential of surface plasmon resonance biosensors in cancer detection," *J. Pharmaceutical Biomed. Anal.*, vol. 194, Feb. 2021, Art. no. 113802, doi: 10.1016/j.jpba.2020.113802.

[29] Y. Singh, M. K. Paswan, and S. K. Raghuwanshi, "Sensitivity enhancement of SPR sensor with the black phosphorus and graphene with bi-layer of gold for chemical sensing," *Plasmonics*, vol. 16, no. 5, pp. 1781–1790, Oct. 2021, doi: 10.1007/s11468-020-01315-3.

[30] M. Mahmoudpour, J. E. N. Dolatabadi, M. Torbati, and A. Homayouni-Rad, "Nanomaterials based surface plasmon resonance signal enhancement for detection of environmental pollutions," *Biosensors Bioelectron.*, vol. 127, pp. 72–84, Feb. 2019, doi: 10.1016/j.bios.2018.12.023.

[31] M. R. Islam, M. M. I. Khan, R. Al Rafid, F. Mehjabin, M. S. Rashid, J. A. Chowdhury, N. Zerin, and M. Islam, "Trigonal cluster-based ultra-sensitive surface plasmon resonance sensor for multipurpose sensing," *Sens. Bio-Sensing Res.*, vol. 35, Feb. 2022, Art. no. 100477, doi: 10.1016/j.sbsr.2022.100477.

[32] M. R. Islam, A. N. M. Iftekher, K. R. Hasan, M. J. Nayen, and S. B. Islam, "Dual-polarized highly sensitive surface-plasmon-resonance-based chemical and biomolecular sensor," *Appl. Opt.*, vol. 59, no. 11, p. 3296, 2020, doi: 10.1364/ao.383352.

[33] F. Chiavaioli, D. Santano Rivero, I. Del Villar, A. B. Socorro-Leránoz, X. Zhang, K. Li, E. Santamaría, J. Fernández-Irigoyen, F. Baldini, D. L. A. van den Hove, L. Shi, W. Bi, T. Guo, A. Giannetti, and I. R. Matias, "Ultrahigh sensitive detection of tau protein as Alzheimer's biomarker via microfluidics and nanofunctionalized optical fiber sensors," *Adv. Photon. Res.*, vol. 3, no. 11, Nov. 2022, doi: 10.1002/adpr.202200044.

[34] S. Zhu, Z. Xie, Y. Chen, S. Liu, Y.-W. Kwan, S. Zeng, W. Yuan, and H.-P. Ho, "Real-time detection of circulating tumor cells in bloodstream using plasmonic fiber sensors," *Biosensors*, vol. 12, no. 11, p. 968, Nov. 2022, doi: 10.3390/bios12110968.

[35] A. Hassani and M. Skorobogatiy, "Design of the microstructured optical fiber-based surface plasmon resonance sensors with enhanced microfluidics," *Opt. Exp.*, vol. 14, no. 24, p. 11616, 2006, doi: 10.1364/oe.14.011616.

[36] T. Yang, L. Zhang, Y. Shi, S. Liu, and Y. Dong, "A highly birefringent photonic crystal fiber for terahertz spectroscopic chemical sensing," *Sensors*, vol. 21, no. 5, p. 1799, Mar. 2021, doi: 10.3390/s21051799.

[37] S. I. Azzam, M. F. O. Hameed, R. E. A. Shehata, A. M. Heikal, and S. S. A. Obayya, "Multichannel photonic crystal fiber surface plasmon resonance based sensor," *Opt. Quantum Electron.*, vol. 48, no. 2, pp. 1–11, Feb. 2016, doi: 10.1007/s11082-016-0414-4.

[38] J. Divya and S. Selvendran, "A novel plasmonic sensor using solid core D-shaped negative curvature optical fiber with AU-TiO_2 layer," *Laser Phys.*, vol. 32, no. 11, Nov. 2022, Art. no. 116205, doi: 10.1088/1555-6611/ac967f.

[39] M. E. Rahaman, R. H. Jibon, M. S. Ahsan, F. Ahmed, and I.-B. Sohn, "Glucose level measurement using photonic crystal fiber-based plasmonic sensor," *Plasmonics*, vol. 17, no. 1, pp. 1–11, Feb. 2022, doi: 10.1007/s11468-021-01497-4.

[40] D. Kumar, M. Sharma, and V. Singh, "Surface plasmon resonance implemented silver thin film PCF sensor with multiple—Hole microstructure for wide ranged refractive index detection," *Mater. Today, Proc.*, vol. 62, no. 12, pp. 6590–6595, 2022, doi: 10.1016/j.matpr.2022.04.598.

[41] A. Yasli, H. Ademgil, S. Haxha, and A. Aggoun, "Multi-channel photonic crystal fiber based surface plasmon resonance sensor for multi-analyte sensing," *IEEE Photon. J.*, vol. 12, no. 1, pp. 1–15, Feb. 2020, doi: 10.1109/JPHOT.2019.2961110.

[42] J. Su, G. Xiao, H. Yang, J. Chen, H. Li, X. Liu, Y. Luo, and J. Li, "Highly sensitive multi-channel biosensor for low-interference simultaneous detection," *Nanomaterials*, vol. 13, no. 2, p. 246, Jan. 2023, doi: 10.3390/nano13020246.

[43] K. M. M. Rahman, M. S. Alam, and M. A. Islam, "Highly sensitive surface plasmon resonance refractive index multi-channel sensor for multi-analyte sensing," *IEEE Sensors J.*, vol. 21, no. 24, pp. 27422–27432, Dec. 2021, doi: 10.1109/JSEN.2021.3126624.

[44] D. Pysz, I. Kujawa, R. Stepien, M. Klimczak, A. Filipkowski, M. Franczyk, L. Kociszewski, J. Buzniak, K. Harasny, and R. Buczynski, "Stack and draw fabrication of soft glass microstructured fiber optics," *Bull. Polish Acad. Sci. Tech. Sci.*, vol. 62, no. 4, pp. 667–682, Dec. 2014, doi: 10.2478/bpasts-2014-0073.

[45] N. Zhang, K. Li, Y. Cui, Z. Wu, P. P. Shum, J.-L. Auguste, X. Q. Dinh, G. Humbert, and L. Wei, "Ultra-sensitive chemical and biological analysisviaspecialty fibers with built-in microstructured optofluidic channels," *Lab Chip*, vol. 18, no. 4, pp. 655–661, 2018, doi: 10.1039/c7lc01247k.

[46] N. Takeyasu, T. Tanaka, and S. Kawata, "Metal deposition deep into microstructure by electroless plating," *Jpn. J. Appl. Phys.*, vol. 44, nos. 33–36, pp. 1134–1137, Aug. 2005, doi: 10.1143/jjap.44.l1134.

[47] A. A. Rifat, F. Haider, R. Ahmed, G. A. Mahdiraji, F. R. M. Adikan, and A. E. Miroshnichenko, "Highly sensitive selectively coated photonic crystal fiber-based plasmonic sensor," *Opt. Lett.*, vol. 43, no. 4, p. 891, 2018, doi: 10.1364/ol.43.000891.

[48] B. Li, T. Cheng, J. Chen, and X. Yan, "Graphene-enhanced surface plasmon resonance liquid refractive index sensor based on photonic crystal fiber," *Sensors*, vol. 19, no. 17, p. 3666, Aug. 2019, doi: 10.3390/s19173666.

[49] P. S. Maji and P. Roy Chaudhuri, "A new design for all-normal near zero dispersion photonic crystal fiber with selective liquid infiltration for broadband supercontinuum generation at 1.55 μm," *J. Photon.*, vol. 2014, pp. 1–9, Apr. 2014, doi: 10.1155/2014/728592.

[50] J. Divya and S. Selvendran, "The impact of different background materials in a D-shaped photonic crystal fiber based plasmonic sensor: A comprehensive investigation," *Opt. Quantum Electron.*, vol. 55, no. 6, Jun. 2023, doi: 10.1007/s11082-023-04695-y.

[51] S. Selvendran, J. Divya, A. Sivanantha Raja, A. Sivasubramanian, and S. Itapu, "A reconfigurable surface-plasmon-based filter/sensor using D-shaped photonic crystal fiber," *Micromachines*, vol. 13, no. 6, p. 917, Jun. 2022, doi: 10.3390/mi13060917.

[52] J. Divya, S. Selvendran, A. S. Raja, and A. Sivasubramanian, "Graphene-Au-coated plasmonic sensor based on D-shaped Bezier polygonal hollow core photonic crystal fiber," *Brazilian J. Phys.*, vol. 51, no. 5, pp. 1314–1323, Oct. 2021, doi: 10.1007/s13538-021-00969-6.

[53] M. R. Islam, M. A. Jamil, S. A. H. Ahsan, M. M. I. Khan, F. Mehjabin, J. A. Chowdhury, and M. Islam, "Highly birefringent gold-coated SPR sensor with extremely enhanced amplitude and wavelength sensitivity," *Eur. Phys. J. Plus*, vol. 136, no. 2, pp. 1–14, Feb. 2021, doi: 10.1140/epjp/s13360-021-01220-6.

[54] M. De and V. K. Singh, "Multi-purpose photonic crystal fiber having advanced optical properties and long sensing range," *Photon. Nanostruct. Fundamentals Appl.*, vol. 36, Sep. 2019, Art. no. 100722, doi: 10.1016/j.photonics.2019.100722.

[55] Q. Liu, S. Li, and H. Chen, "Two kinds of polarization filter based on photonic crystal fiber with nanoscale gold film," *IEEE Photon. J.*, vol. 7, no. 1, pp. 1–11, Feb. 2015, doi: 10.1109/JPHOT.2014.2387262.

[56] M. De, R. K. Gangwar, and V. K. Singh, "Designing of highly birefringence, dispersion shifted decagonal photonic crystal fiber with low confinement loss," *Photon. Nanostruct. Fundamentals Appl.*, vol. 26, pp. 15–23, Sep. 2017, doi: 10.1016/j.photonics.2017.06.002.

[57] C. Li, B. Song, Y. Guo, J. Wu, W. Huang, X. Wu, C. Jin, and S. Chen, "Two modes excited SPR sensor employing gold-coated photonic crystal fiber based on three-layers air-holes," *IEEE Sensors J.*, vol. 20, no. 11, pp. 5893–5899, Jun. 2020, doi: 10.1109/JSEN.2020.2972031.
[58] A. Yasli and H. Ademgil, "Multianalyte sensing analysis with multi-layer photonic crystal fiber-based surface plasmon resonance sensor," *Mod. Phys. Lett. B*, vol. 34, no. 33, Nov. 2020, Art. no. 2050375, doi: 10.1142/s0217984920503753.
[59] S. Singh and Y. K. Prajapati, "Dual-polarized ultrahigh sensitive gold/MoS_2/graphene based D-shaped PCF refractive index sensor in visible to near-IR region," *Opt. Quantum Electron.*, vol. 52, no. 1, Jan. 2020, doi: 10.1007/s11082-019-2122-3.
[60] H. Yang, M. Liu, Y. Chen, L. Guo, G. Xiao, H. Liu, J. Li, and L. Yuan, "Highly sensitive graphene-Au coated plasmon resonance PCF sensor," *Sensors*, vol. 21, no. 3, p. 818, Jan. 2021, doi: 10.3390/s21030818.
[61] B. Lahiri, S. G. Mcmeekin, R. M. De La Rue, and N. P. Johnson, "Resonance hybridization in nanoantenna arrays based on asymmetric split-ring resonators," *Appl. Phys. Lett.*, vol. 98, no. 15, pp. 2012–2015, Apr. 2011, doi: 10.1063/1.3579537.
[62] B. K. Paul, K. Ahmed, S. Asaduzzaman, and M. S. Islam, "Folded cladding porous shaped photonic crystal fiber with high sensitivity in optical sensing applications: Design and analysis," *Sens. Bio-Sensing Res.*, vol. 12, pp. 36–42, Feb. 2017, doi: 10.1016/j.sbsr.2016.11.005.
[63] A. Jalil, S. Ashfaq, D. Bokov, A. Alanazi, K. Hachem, W. Suksatan, and M. Sillanpää, "High-sensitivity biosensor based on glass resonance PhC cavities for detection of blood component and glucose concentration in human urine," *Coatings*, vol. 11, no. 12, p. 1555, Dec. 2021, doi: 10.3390/coatings11121555.
[64] E. Haque, A. A. Noman, and F. Ahmed, "Numerical investigation of photonic crystal fiber-based biosensor for pathogens detection in water," *IEEE Access*, vol. 10, pp. 88885–88893, 2022, doi: 10.1109/ACCESS.2022.3201020.
[65] B. Murshed, L. Mj, and D. As, "Annals of thyroid research design and performance analysis of simple PCF based sensor with high sensitivity for sensing the presence of bacteria-*Pseudomonas aeruginosa*," *Ann. Thyroid Res.*, vol. 8, no. 1, pp. 360–367, 2022.
[66] N. M. Reddy, D. Kothandan, S. C. Lingam, and A. Ahmad, "A study on refractive index of plasma of blood of patients suffering from tuberculosis," *Int. J. Innov. Technol. Creat. Eng.*, vol. 2, no. 8, p. 23, 2012.
[67] A. Yasli, "Cancer detection with surface plasmon resonance-based photonic crystal fiber biosensor," *Plasmonics*, vol. 16, no. 5, pp. 1605–1612, Oct. 2021, doi: 10.1007/s11468-021-01425-6.
[68] P. Manickam and R. Senthil, "Numerical investigation of side-polished SPR PCF sensor for urine analysis," *Plasmonics*, vol. 17, no. 5, pp. 2023–2030, Oct. 2022, doi: 10.1007/s11468-022-01688-7.
[69] M. Abdelghaffar, Y. Gamal, R. A. El-Khoribi, W. Soliman, Y. Badr, M. F. O. Hameed, and S. S. A. Obayya, "Highly sensitive V-shaped SPR PCF biosensor for cancer detection," *Opt. Quantum Electron.*, vol. 55, no. 5, pp. 1–20, May 2023, doi: 10.1007/s11082-023-04740-w.
[70] P. Manickam and R. Senthil, "Numerical demonstration of photonic quasi-crystal fiber–surface plasmonic resonance urinary methanol sensor," *Plasmonics*, vol. 18, no. 2, pp. 511–519, Apr. 2023, doi: 10.1007/s11468-022-01768-8.

J. DIVYA received the B.E. degree in electronic and communication engineering and the M.E. degree in optical communication. She is currently pursuing the Ph.D. degree in photonic crystal fiber-based plasmonic sensors for biosensing applications with the School of Electronics Engineering, Vellore Institute of Technology, Chennai. Her research interests include optics and photonics, including areas such as photonic crystal-based sensors and filters, as well as photonic crystal fiber-based polarization filters utilizing surface plasmon resonance (SPR).

S. SELVENDRAN received the B.E. degree in electronics and communication engineering, the M.E. degree in optical communication, and the Ph.D. degree in information and communication engineering with a focus on nonlinear fiber optics.

He is currently an Associate Professor with the School of Electronics Engineering, Vellore Institute of Technology, Chennai, bringing with him a decade of valuable experience in both teaching and research. In addition to his academic role, he is actively engaged with the Centre for Healthcare Advancement, Innovation, and Research (CHAIR), where his research is dedicated to biosensors. He has a prolific publication record, with 67 research articles to his name, many of which have been featured in renowned international journals (SCI/SCIE/WOS: 38) and international/national conferences. His expertise spans various aspects of optics and photonics, encompassing optical modulation formats, optical fiber design, fiber nonlinearity, optical amplifiers, free-space optics (FSO), visible light communication (VLC), photonic crystal fiber (PCF)-based sensors, and PCF-based polarization filters using surface plasmon resonance (SPR), among others. He has demonstrated his innovative prowess by filing a patent (IPR) related to fiber optic grating. His research interests include photonic crystal devices, specifically focusing on photonic crystal-based fiber, filters, and biosensors.

SRIKANTH ITAPU received the B.Tech. degree in electronics and communication engineering, the M.Tech. degree in laser and electro-optics, and the Ph.D. degree in electrical engineering from the University of Toledo, Toledo, OH, USA.

He was a Postdoctoral Researcher with the University of Toledo before returning to India. He is currently the Chair of the Department of ECE, Alliance University. He has published over 35 scientific articles and is a freelance speaker on nano-electronic devices and sensors for Industry 4.0. His research interests include nano-electronic device fabrication and characterization, RF and microwave, computational first principles studies on novel complex oxides and perovskites, and novel supercapacitor materials for EVs.

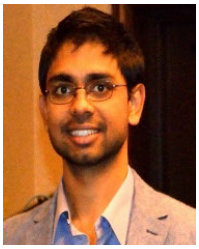

VAMSI BORRA (Senior Member, IEEE) received the bachelor's degree in electronics and communication engineering from Jawaharlal Nehru Technological University, the master's degree in electrical and computer engineering from Youngstown State University (YSU), and the Ph.D. degree in electrical engineering from the University of Toledo. He is currently an Assistant Professor with YSU. Prior to YSU, he was an Assistant Professor and a Program Coordinator with the Department of Computer Science, Information Systems, and Engineering Technology, California University of Pennsylvania (CALU). Prior to CALU, he was a Visiting Assistant Professor with the Electrical Engineering and Computer Science (EECS) Department, University of Toledo. He was an Electrical Engineer with Valley Electrical Consolidated Inc., Girard, OH, USA, before starting the Ph.D. studies. His research interests include whiskers, material characterization, semiconductors, surface plasmon polariton, and thin films.